High-Order Accurate Methods for Time-domain Electromagnetics

J. S. Hesthaven[1] and T. Warburton[2]

Abstract: We discuss the formulation, validation, and parallel performance of a high-order accurate method for the time-domain solution of the three-dimensional Maxwell's equations on general unstructured grids. Attention is paid to the development of a general discontinuous element/penalty approximation to Maxwell's equations and a locally divergence free form of this. We further discuss the motivation for using a nodal Lagrangian basis for the accurate and efficient representation of solutions and operators. The performance of the scheme is illustrated by solving benchmark problems as well as large scale scattering applications.

keyword: Time-domain CEM, Maxwell's equations, high-order accurate methods, unstructured grids, parallel computing.

1 Introduction

The increasing interest in the modeling and design of emerging technologies such as very low observable vehicles, ground/foliage penetrating radars, and phase sensitive components, imposes requirements on the accuracy and performance of the computational tools well beyond that of existing techniques. The eminent need to identify new approaches to electromagnetic modeling and design is further emphasized by the requirements to accurately model the interaction of very broad band signals with electrically large and geometrically complex objects, often including regions of inhomogeneous, anisotropic, lossy materials.

While frequency domain methods are less appealing for the modeling of such problems due to the complexity associated with broad band applications and the inclusion of complex realistic multilayered material models, most current time-domain methods remain 2nd order accurate

at best. This severely limits their ability to correctly represent wave motion over long distances unless the grid is prohibitively fine. Furthermore, most standard techniques, i.e., the finite-difference time-domain method [Taflove (1995); Nambura, Mark and Clarke (2004)] in particular and the finite-volume/finite-element methods [Mohammadian, Shankar and Hall (1991); Rao (1999)] to a lesser extent, suffer from an inability to accurately and efficiently represent complex geometries. Several recent efforts have been aimed at addressing the shortcomings of the classical FDTD schemes, e.g., embedding schemes to overcome staircasing [Ditkowski, Dridi, and Hesthaven (2001)] and high-order finite difference schemes [Turkel and Yefet (2000); Yefet and Petropoulos (2001); Yefet and Turkel (2000); Xie, Chan and Zhang (2002)]. However, these technqiues largely remain experimental. In the context of finite element methods, recent years has seen a number of developments, both of low [Hassan, Morgan, Jones, Larwood, and Weatherill (2004)] and high-order accuracy [Castillo, Koning, Rieben, and White (2004)]. While these are well suited to deal with complex geometries, they become implicit, at higher than 2nd order accuracy. Efforts to address this by proposed fast and accurate time-advancement methods are discussed in [Jose, Kanapady, and Tamma (2004)] and references therein.

For the accurate modeling of large scale scattering and penetration applications the shortcomings of low order methods render them impractical. However, understanding the source of the problems also suggest that a high-order time-domain solution technique may offer the efficiency and accuracy required for future large scale CEM modeling capabilities. High-order methods, with spectral methods representing the ultimate limit, are characterized by being able to accurately represent wave propagation over very long distances, using only a few points per wavelength and with an error accumulation rate that is significantly reduced as compared to 2nd order accurate schemes [Kreiss and Oliger (1972)]. For three-dimensional large scale computations, this translates into

---

[1] Division of Applied Mathematics, Brown University, Providence, RI 02912. Email: JAN.HESTHAVEN@BROWN.EDU

[2] Department of Mathematics and Statistics University of New Mexico, Albuquerque, NM 87131. Email: TIMWAR@MATH.UNM.EDU

dramatic reductions in the required computational resources, i.e., memory and execution time, and promises to offer the ability to model problems of a realistic complexity and size.

Traditionally, the development of suitable high-order solution techniques has been held back by the difficulties associated with formulating stable and high-order accurate schemes for solving wave-dominated problems in geometrically complex domains. The recent development of stable discontinuous element/Penalty methods [Cockburn and Shu (2001); Hesthaven (2000)] and efficient and accurate ways of representing solutions and operators on simplices [Hesthaven and Gottlieb (1999); Hesthaven and Teng (2000); Hesthaven and Warburton (2002)] has paved the way for overcoming these restrictions associated with classical high-order methods. In contrast to high-order schemes based on classical finite element techniques, the approach taken here leads to fully explicit schemes.

As we shall discuss further, the combination of these results enables us to formulate and implement geometrically flexible, high-order accurate and computationally efficient and robust methods for the time-domain solution of Maxwell's equations. Efforts of a similar flavor, yet with several distinct differences are described in [Kopriva, Woodruff and Hussaini (2000); Kopriva, Woodruff, and Hussaini (2002); Warburton (2000)].

2   The Physical Problem

We shall consider the solution of Maxwell's equations in the general domain, Ω, in the scattered field formulation

$$\varepsilon \frac{\partial E^s}{\partial t} = \nabla \times H^s + \sigma E^s + S^E \ , \tag{1}$$

$$\mu \frac{\partial H^s}{\partial t} = -\nabla \times E^s + S^H \ , \tag{2}$$

$$\nabla \cdot \varepsilon E^s = \rho \ , \ \ \nabla \cdot H^s = 0 \ , \tag{3}$$

where E^s and H^s signify the scattered electric and magnetic fields, respectively, ε and μ represents the local permittivity and permeability, and ρ is the space charge. The source terms take the form

$$S^E = -\left(\varepsilon - \varepsilon^i\right)\frac{\partial E^i}{\partial t} + (\sigma - \sigma^i)E^i \ , \tag{4}$$

$$S^H = -\left(\mu - \mu^i\right)\frac{\partial H^i}{\partial t} \ , \tag{5}$$

where $\varepsilon^i(x)$, $\mu^i(x)$, and $\sigma^i(x)$ represent the permittivity, permeability, and conductivity of the media in which the incident field, (E^i, H^i), is a solution to Maxwell's equations.

In all subsequent computations we assume that Eqs.(1)-(2) are normalized such that the vacuum speed of light is unity, i.e., $\varepsilon_0 = \mu_0 = 1$, all lengths are scaled with respect to a chosen length scale, and the electric fields are scaled with the vacuum intrinsic capacitance. We shall also assume that that the incident field is a vacuum solution, i.e., $\varepsilon^i = \mu^i = 1$, and $\sigma^i = 0$.

Along the interface of any two dielectric bodies, endowed with an outward pointing normal vector, $\hat{n}$, the tangential field components remain continuous, i.e.,

$$\hat{n} \times (E^s_1 - E^s_2) = 0 \ , \ \ \hat{n} \times (H^s_1 - H^s_2) = 0 \ , \tag{6}$$

everywhere. At a perfect electric conductor, on the other hand, the fields are unable to penetrate the body and the conditions are

$$\hat{n} \times E^s = -\hat{n} \times E^i \ , \ \ \hat{n} \cdot H^s = -\hat{n} \cdot H^i \ , \tag{7}$$

indicating that the total tangential electric and normal magnetic field components must vanish to enforce no penetration.

3   The Computational Scheme

We shall seek approximate solutions to Maxwell's equations in a general domain, Ω, containing a collection of scattering bodies. To facilitate the required geometric flexibility, we represent the computational domain as the union of K non-overlapping body-conforming tetrahedra, D.

This decomposition introduces two issues that will need attention, i.e., how to represent the fields and in which way these approximate fields are required to satisfy Maxwell's equations. In the following we shall discuss this in more some detail, albeit in the reverse order.

3.1 The Penalty Formulation

As is common, we assume that Eq.(3) is satisfied by the initial conditions and only consider the solution of Eqs.(1)-(2). In Sec. 3.1.1 we shall, however, return to this issue.

Let us express Maxwell's equations, Eqs.(1)-(2), in conservation form

$$Q(x)\frac{\partial q}{\partial t} + \nabla \cdot F(q) = S(q^i, x) \quad , \tag{8}$$

where we have introduced the state vector, q, and the flux $F(q) = [F_1(q), F_2(q), F_3(q)]^T$, as

$$q = \begin{bmatrix} E \\ H \end{bmatrix} \quad , \quad F_i(q) = \begin{bmatrix} -\hat{e}_i \times H \\ \hat{e}_i \times E \end{bmatrix} \quad .$$

respectively. Here $\hat{e}_i$ signifies the three Cartesian unit vectors. We also have the material coefficient matrix, $Q = \text{diag}(\varepsilon, \varepsilon, \varepsilon, \mu, \mu, \mu)$, and the source, $S = [S^E, S^H]^T$, depending on the incident field, $q^i = [E^i, H^i]^T$.

To formulate the scheme, let us assume that there exists an approximate solution, $q_N \in P_n$, on the form

$$\forall x \in D \; : \; q(x,t) \simeq q_N(x,t) = \sum_{i=1}^{N} \hat{q}_i(t)\psi_i(x) , \tag{9}$$

within each tetrahedron. Similarly, we assume that F_N and S_N are polynomial representations of the flux and of the source, respectively.

Throughout, we use P_n to signify the minimal polynomial space for approximation on the tetrahedron, i.e., $P_n = \text{span}\{x^{\alpha_1} y^{\alpha_2} z^{\alpha_3}\}_{|\alpha| \le n} = \text{span}\{\psi_i\}_{i=1}^{N}$ with $\alpha = (\alpha_1, \alpha_2, \alpha_3)$ being a multi-index, and

$$\dim P_n = N = \frac{(n+1)(n+2)(n+3)}{6} \quad ,$$

are the number of unknowns on each element.

To seek equations for these N unknowns, we require the approximate solution to Maxwell's equations, q_N, to satisfy

$$\int_D \left(Q\frac{\partial q_N}{\partial t} + \nabla \cdot F_N - S_N \right) \Phi_i(x)\, dx$$

$$= \oint_{\delta D} \Psi_i(x)\hat{n} \cdot [F_N - F^*]\, dx \quad . \tag{10}$$

Here Φ_i and Ψ_i represent sequences of N test functions, F^* signifies a numerical flux and $\hat{n}$ is an outward pointing unit vector defined at the boundary of the element. If the numerical flux is consistent, the scheme is clearly consistent. On the other hand, boundary/interface conditions are not imposed exactly but rather weakly through the penalizing surface integral. Within this multi-element context, the formulation is inherently discontinuous and yields, through its very construction, a highly parallel local scheme.

Let us for simplicity assume that the materials can be taken to be constant on each element, i.e., Q is constant, and also that all sides of the tetrahedron are planar. Introducing the operators

$$\hat{M}_{ij} = \int_D \psi_j \Phi_i\, dx \; , \; \hat{S}_{ij} = \int_D \nabla\psi_j \Phi_i\, dx \; , \tag{11}$$

$$\hat{F}_{ij} = \oint_{\delta D} \Psi_i \psi_j\, dx \; , \tag{12}$$

transforms Eq.(10) into the explicit scheme

$$Q\hat{M}\frac{d\hat{q}}{dt} + \hat{S} \cdot \hat{F} - \hat{M}\hat{S} = \hat{F}\hat{n} \cdot [\hat{F} - \hat{F}^*] \quad . \tag{13}$$

where $\hat{q}$ represents the 6N-vector of coefficients for q_N, and similarly for $\hat{F}$, $\hat{S}$, and $\hat{F}^*$ for the flux, the source, and the numerical flux, respectively.

In choosing Φ_i, Ψ_i and the numerical flux, F^*, one has a large degree of freedom in designing schemes suitable for solving conservation laws. Here we focus on the Galerkin formulation in which case $\Psi_i(x) = \Phi_i(x) = \psi_i(x)$. It is worth noting that after integration by parts in Eq.(10) this scheme becomes the much studied discontinuous Galerkin method [Cockburn and Shu (2001)]. This is, however, only one among numerous formulations in the same family of discontinuous element/Penalty methods. We refer to [Hesthaven (2000); Hesthaven and Gottlieb (1999); Hesthaven and Teng (2000)] for examples and further references.

To finalize the formulation of the scheme, we need to specify the numerical flux, F^*, which is responsible for passing information between the elements and imposing the boundary conditions. Given the linearity of Maxwell's equations, it is natural to use upwinding through characteristics to obtain [Mohammadian, Shankar and Hall (1991)]

$$\hat{n} \cdot [F - F^*] = \begin{cases} \overline{Z}^{-1} n \times (n \times [E] - Z^+[H]) \\ \overline{Y}^{-1} n \times (n \times [H] + Y^+[E]) \end{cases} , \quad (14)$$

where $[q] = q^- - q^+$ measures the jump in the field values across an interface. Superscript '+' refers to field values from the neighbor element while superscript '-' refers to field values local to the element. To account for the potential differences in material properties in the two elements, we have introduced the local impedance, $Z^\pm$, and conductance, $Y^\pm$, defined as

$$Z^\pm = \frac{1}{Y^\pm} = \sqrt{\frac{\mu^\pm}{\varepsilon^\pm}} ,$$

and the sums

$$\overline{Z} = Z^+ + Z^- , \quad \overline{Y} = Y^+ + Y^- ,$$

of the local impedance and conductance, respectively.

The simplicity of the scheme, Eq.(13), allows a full semi-discrete convergence analysis with the central result

$$\|q(t) - q_N(t)\|_{L^2(\Omega)} \le C \frac{h^\sigma}{n^p} \left[1 + C(T) \frac{n^{3/2}}{h} t \right] \|q(0)\|_{H^p(\Omega)}$$

where $0 \le t \le T$ and $p \ge 3/2$. Here h signifies the maximum edge length, $\sigma = \max(n+1, p)$ and $\| \cdot \|_{L^2(\Omega)}$ and $\| \cdot \|_{H^p(\Omega)}$ represent the broken L^2 and Sobolev-p norm, respectively.

This result confirms convergence in an hp-sense, i.e., one can resolve the solution by refining the grid, h-convergence, and/or increasing the order of the scheme, p-convergence, provided the solution is sufficiently smooth. Furthermore, the error can grow at most linearly with the growth rate controlled by the resolution. The details of the analysis can be found in [Hesthaven and Warburton (2002)].

3.1.1 A Locally Divergence Free Formulation

When deriving the scheme, Eq.(13), we neglected the divergence conditions on the fields, Eq.(3), relying on the observation that Eq.(3) is a condition on the initial conditions to Eqs.(1)-(2). The scheme in Eq.(13) does not

solve Eqs.(1)-(2), however, but rather an approximation to it. Hence, one needs to consider the question of how well Eq.(13) conserves the divergence.

Simply using the convergence result given above, one easily shows [Hesthaven and Warburton (2002)]

$$\|\nabla \cdot q_N(t)\|_{L^2(\Omega)} \le \frac{h^{\sigma-1}}{n^{p-1}} \left[1 + C(T) \frac{n^{5/2}}{h} t \right] \|q(0)\|_{H^p(\Omega)}$$

provided $q \in H^p(\mathrm{D})$, $p \ge 7/2$. Thus, one still have control over the divergence error by the resolution, provided the solution is sufficiently smooth. However, for some applications, in particular when computing at low order, this may not be acceptable.

It is, however, possible to reformulate the scheme to recover a formulation that locally conserves the divergence of the initial conditions to machine accuracy. In doing so, we will need to assume that all tetrahedra have straight faces only. While this may not be true in some computations, the number of elements with curved faces will be a small fraction of the total number of the elements. Hence, the impact of violating this assumption will be small if any.

To recover a locally divergence free formulation, we must first recognize that a discrete divergence operator, D, can be given as

$$\hat{q}' = \hat{M}^{-1} \hat{S} \cdot \hat{q} = \hat{D} \cdot \hat{q} .$$

This follows directly from the definition of the operators in Eqs.(11)-(12), the fact that we are working with polynomials and assuming that all integrations are done exactly.

Now recall that Eq.(13) is a linear problem which, for simple elements, has no mechanism for generating aliasing errors. Taking the divergence of Eq.(13) yields

$$Q \frac{d\hat{D} \cdot \hat{q}}{dt} + \hat{D} \cdot \hat{M}^{-1} \hat{S} \cdot \hat{F} - \hat{D} \cdot \hat{S} = \hat{D} \cdot \hat{M}^{-1} \hat{F} n \cdot [\hat{F} - \hat{F}^*] .$$

Recall that, $\hat{D} \cdot \hat{F} = \hat{D} \times \hat{q}$, is the discrete representation of the rotation operator. Thus, for $F_N \in P_n$, which is true under the assumption of linearity, straight faced tetrahedra and piecewise constant materials, we recover that

$$\hat{D} \cdot \hat{D} \times \hat{q} = 0 \ ,$$

to machine precision as in the continuous case. Furthermore, from Eqs.(4)-(5) we see that $D \cdot \hat{S} = 0$ provided only that the initial conditions, or rather its polynomial representation, is divergence free and that $\rho = 0$.

This implies that we can isolate the source of generation of divergence since

$$Q \frac{d\hat{D} \cdot \hat{q}}{dt} = \hat{D} \cdot \hat{M}^{-1} \hat{F} n \cdot [\hat{F} - \hat{F}^*] \ ,$$

i.e., it is originating from the weakly imposed fluxes at the interfaces and boundaries.

This also suggests that a locally divergence free solution can be recovered by considering the following problem

$$Q\hat{M} \frac{d\hat{q}}{dt} + \hat{S} \cdot \hat{F} - \hat{M}\hat{S} = \hat{F} n \cdot [\hat{F} - \hat{F}^*] \ ,$$
$$Q\hat{M} \frac{d\hat{p}}{dt} + \hat{S} \cdot \hat{F} - \hat{M}\hat{S} = 0 \ , \tag{15}$$

where $\hat{p}$ is a solution, evolved in tandem with the original solution and at no additional computational expense, with the divergence of the initial conditions.

In the special case of $\rho = 0$, one can use $p_N = [E_N, H_N]^T$ to recover divergence free approximations to both fields. In the general case, $p_N = H_N$, provides a locally divergence free approximation to H. This is, however, generally less accurate that $\hat{q}$ due to the missing boundary term in the equation for $\hat{p}$.

3.2 The Nodal Element

To complete the description of the scheme, Eq.(13) or Eq.(15), we need to specify the polynomial basis, $\psi_i(x)$, and define the expansion coefficients, $\hat{q}$.

We limit the complexity by introducing a standard tetrahedron,

$$I = \left\{ (\xi, \eta, \zeta) \in R^3 | (\xi, \eta, \zeta) \geq -1; \xi + \eta + \zeta \leq 1 \right\} \ .$$

We assume that a smooth mapping, $\Pi : I \to D$, exists between I and any general tetrahedron, D. Let $J(\xi)$ signify

the non-singular transformation Jacobian which enables us to compute all operators, Eqs.(11)-(12), by integration on I. It is worth recalling that for any straight faced tetrahedron, J will be constant, i.e., one needs only compute and store the discrete operators on I as all others follow by linear scaling.

In this setting, we begin by considering the appropriate choice of the basis. An immediate candidate is the monomial basis, $\psi_i(x) = x^{\alpha_1} y^{\alpha_2} z^{\alpha_3}$ with $|\alpha| \leq n$. As is well known, however, this will lead to extremely illconditioned operators as the basis becomes almost linearly dependent for high polynomial order and prohibits the stable and accurate computation at high order.

The way to overcome such conditioning problems is to seek an orthonormal basis on I. Such a basis has been known for a long time [Proriol (1957); Koornwinder (1975)]

$$\tilde{\psi}_i(\xi) = P_{\alpha_1}^{(0,0)}(r) \left(\frac{1-s}{2} \right)^{\alpha_1}$$
$$\times P_{\alpha_2}^{(2\alpha_1+1,0)}(s) \left(\frac{1-t}{2} \right)^{\alpha_1+\alpha_2} P_{\alpha_3}^{(2\alpha_1+2\alpha_2+2,0)}(t) \ ,$$
$$\gamma_i = \frac{2}{2\alpha_1+1} \frac{2}{2(\alpha_1+\alpha_2)+2} \frac{2}{2(\alpha_1+\alpha_2+\alpha_3)+3} \ ,$$

$$\psi_i(\xi) = \frac{\tilde{\psi}_i(\xi)}{\sqrt{\gamma_i}} \ , \tag{16}$$

where

$$r = -\frac{2(1+\xi)}{\eta+\zeta} - 1 \ , \quad s = \frac{2(1+\eta)}{1-\zeta} - 1 \ , \quad t = \zeta \ ,$$

and $P_n^{(\alpha,\beta)}(x)$ represents the classical Jacobi polynomial of order n [Szegö (1939)].

This leaves the question of how to compute the expansion coefficients, $\hat{q}$. Clearly, with an orthonormal basis at hand, it may seem natural to exploit the orthonormality to define $\hat{q}$. The impact of doing so is that all modes are needed to evaluate q_N pointwise. This lack of separation between inner modes and boundary modes is not optimal for the current formulation where the flux term in Eq.(13) depends on the fluxes at the boundary of D only. To overcome this issue, which can impact the performance as

discussed shortly, one could seek to give up the strict orthonormality of the basis to achieve a separation between inner and boundary modes. Such a basis, which share a number of similarities with Eq.(16), is discussed in [Karniadakis and Sherwin (1999)] and provides an approach, albeit rather complex, to achieve arbitrarily high order accuracy.

Here we take a different approach and define $\hat{q}$ such that q_N is an interpolating polynomial, i.e., we require that

$$\forall i \,:\, q_N(\xi_i,t) = \sum_{j=1}^{N} \hat{q}_j(t)\psi_j(\xi_i) \;,$$

where $\psi_j(\xi)$ is the orthonormal basis in Eq.(16) and ξ_i are N predefined grid-points in I. On vector form this becomes

$$q_N = \mathrm{V}\hat{q} \;,\;\; \mathrm{V}_{ij} = \psi_j(\xi_i) \;, \tag{17}$$

where V is a multidimensional Vandermonde matrix. This allows us to define a genuine multivariate Lagrangian basis as

$$q_N(\xi,t) = \sum_{i=1}^{N} q_N(\xi_i,t)L_i(\xi) \;,\;\; \mathrm{V}^T L = \psi \;,$$

where the latter expression for evaluation of the Lagrange polynomials follows from the interpolation property. Here $L = [L_1(\xi),..,L_N(\xi)]^T$ and the basis is given as $\psi = [\psi_1(\xi),..,\psi_N(\xi)]^T$.

The final issue in need of attention is the choice of the nodal points, ξ_i, within I. As is well known, the success of high-order Lagrangian interpolation is critically dependent on the correct distribution of the nodes. This is a problem that has received some attention recently and nodal distributions, allowing for the construction of well behaved unique Lagrange polynomials up to order 10, can be found in [Chen and Babuška (1996); Hesthaven and Teng (2000)].

The nodal distributions are characterized by having exactly N nodes. Furthermore, the nodal set includes the vertices, the edges, and the faces of the tetrahedron. The number of nodes on each face is exactly that is required to support a two-dimensional multivariate polynomial, i.e., $N_{2d} = (n+1)(n+2)/2$ nodes on each face.

In this framework, it is more natural to recast the scheme in physical space rather than in modal space as given in Eq.(13). Using the identity in Eq.(17) and multiplying Eq.(13) with $(\mathrm{V}^{-1})^T$ from the left yields

$$\mathrm{QM}\frac{dq_N}{dt} + \mathrm{S} \cdot F_N - \mathrm{M}S_N = \mathrm{F}n \cdot [F_N - F^*] \;. \tag{18}$$

Here we have q_N, F_N, S_N, and F^* representing the 6N-vector of nodal values in physical space of the solution, the flux, the source, and the numerical flux, respectively.

The discrete, pointwise operators, are given as

$$\mathrm{M}_{ij} = \int_{\mathrm{D}} L_i L_j\, dx \;,\;\; \mathrm{M} = \left(\mathrm{V}\mathrm{V}^T\right)^{-1} \;, \tag{19}$$

$$\mathrm{S}_{ij} = \int_{\mathrm{D}} L_i \nabla L_j\, dx \;,\;\; \mathrm{S} = (\mathrm{V}^{-1})^T \hat{\mathrm{S}} \mathrm{V}^{-1} \;, \tag{20}$$

where the modal operators are given in Eqs.(11). The form of the boundary operator, F, is simplified as a consequence of the uniqueness of the Lagrange polynomial and the structure of the nodal points, i.e., integration of the three-dimensional L_i over the surface is equivalent to the sum of the integration of the two-dimensional Lagrange polynomials defined by the nodal distribution on the faces. This implies that

$$\mathrm{F}_{ij}^{\mathrm{face}} = \oint_{\mathrm{face}} l_i^{2D} l_j^{2D}\, dx \;, \tag{21}$$
$$\mathrm{F} = \sum_{\mathrm{faces}} \mathrm{R}_{face}^T (\mathrm{V}_{2D}^{-1})^T \mathrm{F}^{\mathrm{face}} \mathrm{V}_{2D}^{-1} \mathrm{R}_{face} \;.$$

Here l_i^{2D} represents the two-dimensional Lagrange polynomials defined by the nodes on each of the 4 faces, V_{2D} is the associated Vandermonde matrix similar to the three-dimensional form, Eq.(17), and R_{face} is an $N_{2d} \times N$ which serves to extract those nodes situated at each face of the element. This reflects the natural separation between internal and boundary nodes.

To reiterate the importance of the separation between internal and boundary nodes, which is immediate when using the nodal element, we note that the operation count for evaluating the scheme, Eq.(13), assuming no separation, is $O(6N^2)$ for each variable. For the nodal scheme, or a modal scheme with a similar separation, the work scales like $O(2N^2 + 4NN_{2d})$. Hence, the relative saving in operations scales as

$$\frac{\text{Work with Nodal Basis}}{\text{Work with Simple Modal Basis}} = \frac{1}{3} + \frac{2}{n+3} \quad .$$

This clearly becomes increasingly important as the order of the approximation, n, increases, although even for $n = 3$ do we find a $1/3$ reduction.

Another important advantage of the nodal element is the ease by which one can relax the restriction on tetrahedra having straight faces only. Clearly, this will impact the evaluation of the discrete operators, Eqs.(11)-(12) and Eqs.(19)-(21), in a similar way by requiring specific operators for each element and sufficient accuracy in the integration to evaluate entries in the operators. However, the evaluation of the boundary fluxes, Eq.(14), is straightforward in a nodal representation even in the normal vectors, $\hat{n}$, have variation along the faces. In a modal representation, this will require convolutions and additional work when setting up the boundary terms.

Number of Processors	64	128	256	512
Relative time	1.00	0.48	0.24	0.14

Table 1 : Relative time for a 245.000 element grid with 6'th order elements as a function of number of processors. All computations performed at IBM SP located at SRC NAVO. One unit time, representing one complete flux evaluation, corresponds to 8.1 sec wall clock time.

3.3 *Parallel Performance*

The discontinuous element formulation discussed above enables a highly efficient parallel implementation on contemporary large scale distributed memory machines. As a verification of this, we list in Table 1 the relative parallel speedup for a single large scale application, and observe superlinear scaling. Similar and more extensive studies, given in [Hesthaven and Warburton (2002)], confirm this high parallel efficiency for a variety of applications.

4 **Verification and Beyond**

In the following we shall present some computational results to verify the performance and high-order accuracy of the given in Eq.(18). We advance the semi-discrete scheme in time using a low-storage 4th order explicit

Runge-Kutta method [Carpenter and Kennedy (1994)] and terminate the computational domain with a combination of stretching of the grid and characteristic boundary conditions at the outer boundaries.
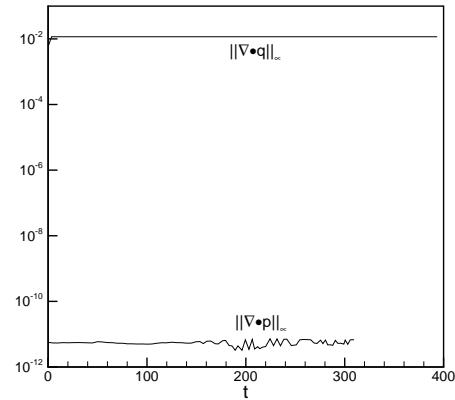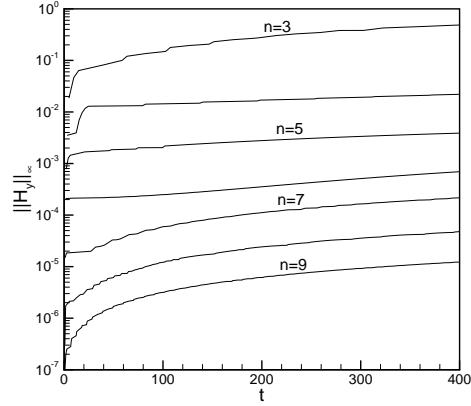

Figure 1 : On top we show the temporal evolution of maximum error for different orders of approximation, n, for a wave captured in a metallic cavity. The bottom figure illustrates the ability to compute a fully divergence free solution, using the divergence free scheme with the extra variable, p. This result is obtained with n=6.

4.1 *Sanity Checks*

As a test of the analysis and basic properties of the scheme, we consider a two-dimensional, 2λ long cavity with metallic end plates and assumed periodicity in y. The cavity is tiled with 8 triangles and a wave is used as initial conditions.

In Fig. 1 we show the temporal evolution of error for different orders of approximation, confirming the expected exponential convergence as control of the growth rate. Also in Fig. 1 we confirm the validity of the divergence free formulation in Eq.(15). While the additional variable, p, provides a divergence free approximation to the solution, it is generally about an order of magnitude less accurate.
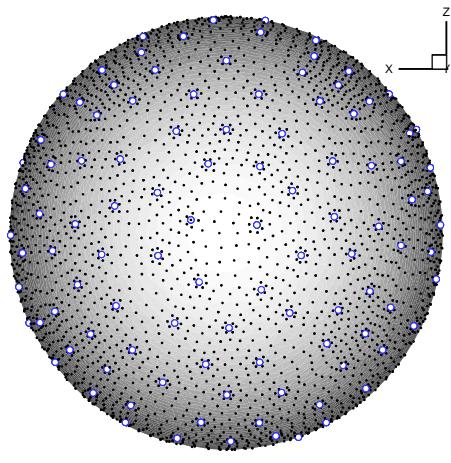

Figure 2 : Example of a body conforming grid of a $ka = 10$ sphere. The open circles signify the vertices of the triangles on the surface and the full dots the local nodes for 6th order elements.

As a first verification of the general three-dimensional framework, let us consider plane wave scattering by a $ka = 10$ perfectly conducting sphere, the analytic solution of which is given by a Mie-series. The surface of the fully bodyconforming grid is illustrated in Fig. 2. The grid has a total of 3000 elements, with an average edge length at the sphere of $4\lambda/5$.

In Fig. 3 we illustrate the convergence of the scheme with a fixed grid when increasing the order of the approximation within each tetrahedron. Even for $n = 3$, i.e., a third order scheme with about 5 points per wavelength, do we compute a reasonable solution while increasing the order yields a rapidly converging solution as one would expect.

4.2 Benchmarks

As an example of a problem, involving penetration, we consider plane wave scattering by a dielectric cylinder, 5λ long, radius of 1 λ and made of a non-magnetic material with a permittivity of $\varepsilon_r = 2.25$, similar to that of
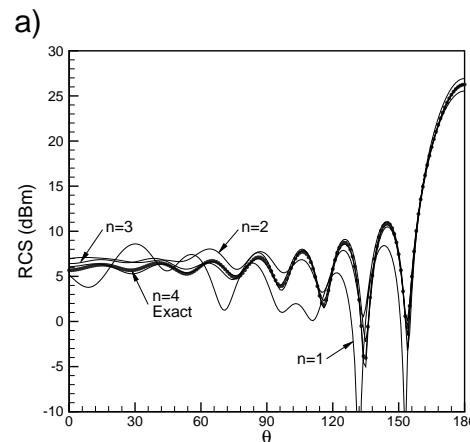

Figure 3 : Plane wave scattering by a $ka = 10$ metallic sphere for a fixed grid and increasing order, n, of the polynomial approximation. We show the convergence of RCS(θ,0) for vertical polarization (TM)
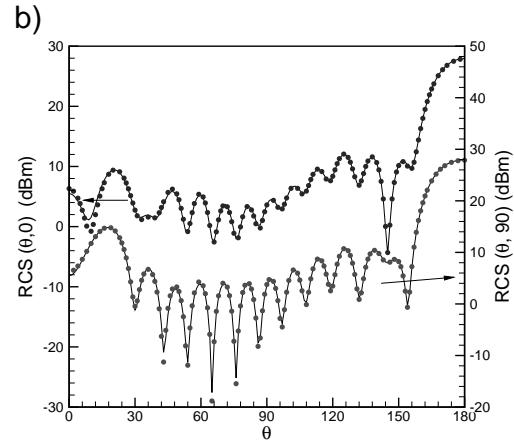

Figure 4 : Scattering by a finite length di-electric cylinder with $\varepsilon_r = 2.25$. We show the RCS(θ,0) for vertical polarization ($\cdot$) of the illuminating field and RCS(θ,90) for horizontal polarization ($\cdot$) compared with results obtained using a pseudospectral axi-symmetric code (full line) [Yang and Hesthaven (1999)]

glass. We find that using a total of approximately 67.000 elements, supporting a 4th order approximation and with an average vacuum edge length at the cylinder of $\lambda/3$, suffices to accurately predict the far field scattering.

In Fig. 4 we show a direct comparison between the full bistatic RCS for a plane wave impinging directly at the

end of the cylinder as computed using the current framework as well as an independently verified pseudospectral multidomain axisymmetric code [Yang and Hesthaven (1999)]. As expected we find an almost perfect agreement between the results of the two schemes over approximately 50 dB dynamical range.
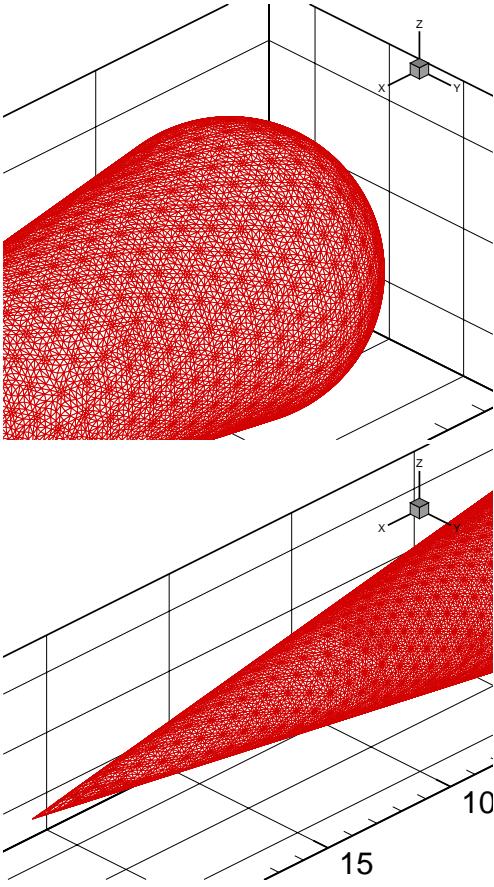

Figure 5 : Details of the body conforming grid used to compute scattering by a large PEC cone-sphere. The surfaces are triangulated for visualization based on the nodes of the high-order elements

As a considerably more challenging benchmark problem, we consider plane wave scattering by a perfectly conducting conesphere, consisting of a 60.5 cm long cone with half angle of 7 deg, capped smoothly with a spherical cap of radius 7.49 cm [Volakis (1992)]. Illuminated by a 9 GHz plane wave, the object is approximately 21 wavelengths long. What makes the problem challenging, though, is not only its electric size but also the very sharp apex and the long shadow region in which surface waves are excited and travel to focus at the apex. Details of

the bodyconforming grid, shown in Fig. 5 illustrated the geometry of the problem.
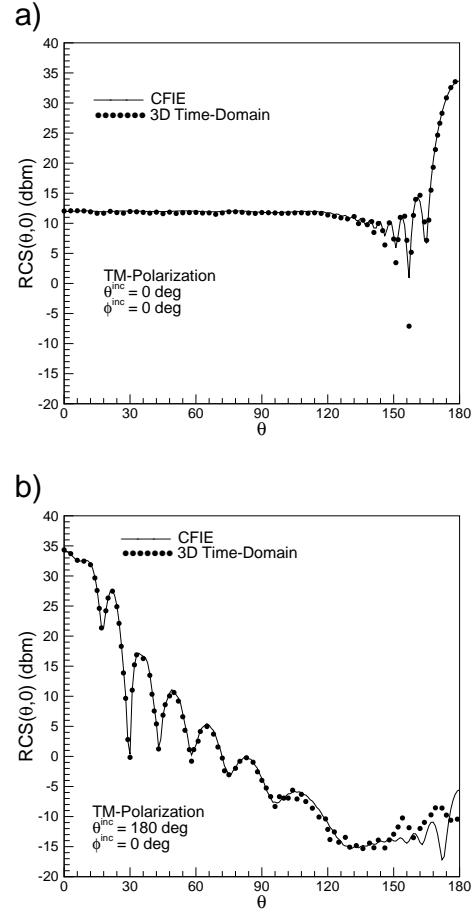

Figure 6 : Plane wave scattering by a metallic cone-sphere illuminated axially by a plane wave. On top we show RCS(θ,0) for incidence on the spherical cap, while the bottom figure shows similar results for RCS(θ,0) for incidence directly at the apex. Both results are for vertical (TM) polarization of the incident wave and compared to results obtained by a CFIE frequency domain solver [Shore (2000)].

In Fig. 6 we show a detailed comparison of the full bistatic cross-section for axial plane wave illumination of the conesphere, showing excellent agreement with high fidelity results obtained using a CFIE integral equation solver with a very high surface resolution. The computation utilizes about 270.000 elements at 3rd order with a resolution at the surface of up to 20 points/wavelength. We note the excellent agreement and a dynamic range ex-
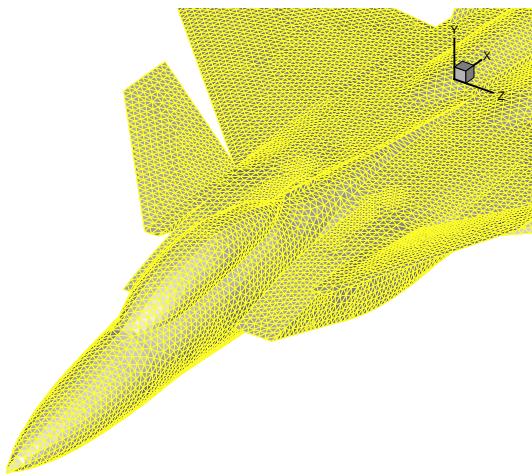
Figure 7 : Details of the surface grid used to compute scattering by a PEC military aircraft. The triangulated surface corresponds to the finite element grid, i.e., each triangle supports a high-order element.

ceeding 50 dB. Similar results and agreement have been found for TE polarized illumination.

4.3 Applications

As a final example of realistic complexity, we consider plane wave scattering by a military aircraft at 600MHz, at which point the aircraft is approximately 50 wavelengths long. The grid consists of 245.000 tetrahedra. A section of the surface grid is shown in Fig. 7.

The aircraft is assumed to be a perfectly conducting metallic shell, and the wave illuminates the aircraft broadside in the plane of the wings. While no computational results or measurements are available for validation of the results, the ability to compute at different orders at the same grid provides a way of establishing convergence of the results. In Fig. 8 we show the bistatic RCS computed a 3 different orders of approximation, $n = 1 - 3$. The results confirm convergence, at least for the 2nd and 3rd order schemes.

An illustration of the surface fields are given in Fig.9 where we show the distribution over the full aircraft.

5   Concluding Remarks

In the paper we have discussed the formulation and validation of a fully unstructured, high-order accurate scheme for the time-domain solution of Maxwell's equa-
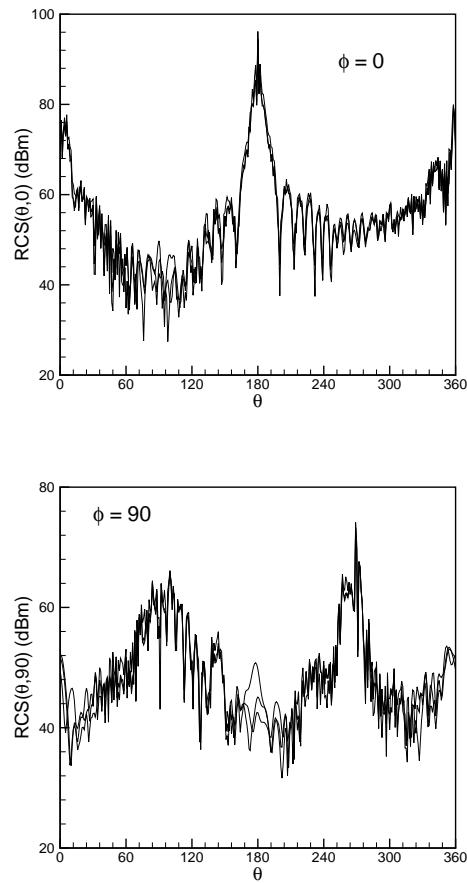

Figure 8 : 600 MHz plane wave scattering by a PEC military aircraft, illuminated broadside by a plane wave. On top we show RCS(θ,0) for and measured in the plane of the wings, while the bottom figure shows equivalent results for RCS(θ,90). Both results are for TE- polarization. Both graphs have results obtained for approximation orders of $n = 1 - 3$, illustrating that the results are converged.

tions. The discussion has focused on the formulation of the scheme and how choices have been made with performance in mind. We have also presented a formulation which enables the strict conservation of the divergence and illustrated the very high parallel performance of the scheme. The evaluations include both standard benchmarks for scattering and penetration as well as nontrivial test cases and confirms the expected accuracy. It should be emphasized that while we have focused on the use of tetrahedra to fill the volume, everything said carries
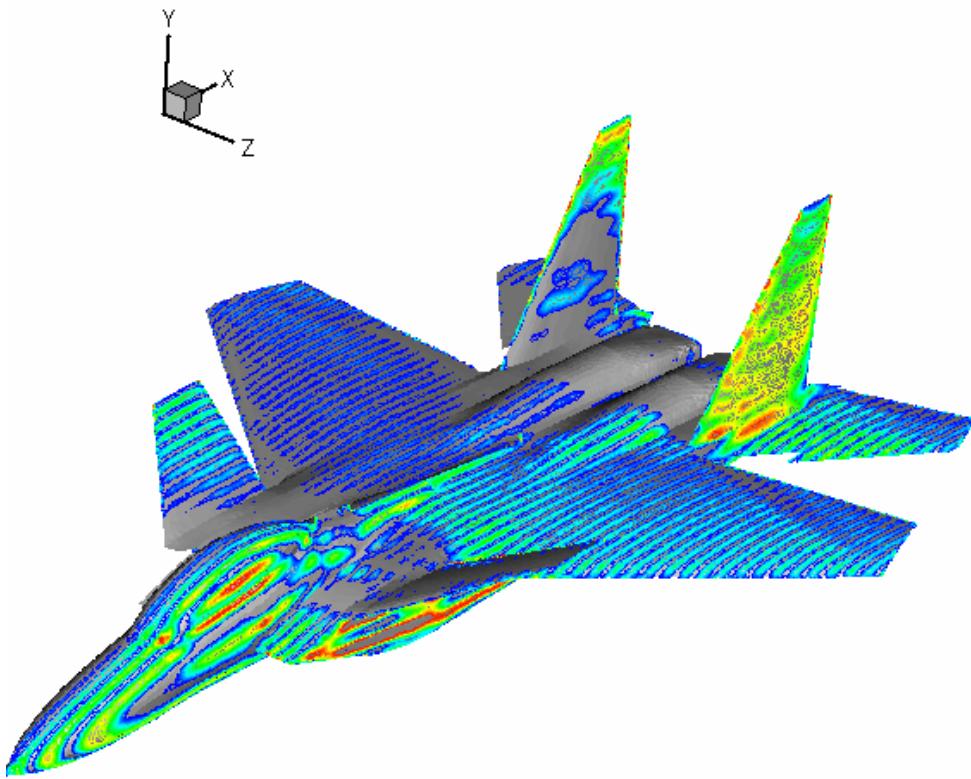
Figure 9 : Field distribution on PEC military aircraft at 600 MHz broadside plane wave illumination.

over to methods based on hexahedra, mixed elements and even custom-designed nodal elements.

While the current framework provides an accurate, geometrically flexible, efficient, and robust computationally kernel for the solution of Maxwell's equations much work is still needed to further expand the capabilities. Particular areas of interest include improved absorbing boundary conditions to increase the dynamic range, mixed implicit/explicit and/or local time-stepping scheme to enable modeling of geometrically small features such as coatings and embedded antennas, and the use of impedance boundary conditions where possible.

References

Carpenter, M. H.; Kennedy, C. A. (1994): Fourth order 2N-storage Runge-Kutta scheme, NASA-TM-109112, NASA Langley Research Center, VA.

Castillo, P.; Koning, J.; Rieben, R.; White, D. (2004): A Discrete Differential Forms Framework for Computational Electromagnetics *CMES: Computer Modeling in Engineering & Sciences*, vol. 5, no. 4, pp. 331-346.

Chen, Q.; Babuška, I. (1996): The Optimal Symmetrical Points for Polynomial Interpolation of Real Functions in a Tetrahedron *Comput. Methods Appl. Mech. Engrg.* **137**, pp. 89-94.

Cockburn, B.; Shu, C. W. (2001): Runge-Kutta Discontinuous Galerkin Methods for Convection-Dominated Problems, *J. Sci. Comput.* **16**, pp. 173-261.

Ditkowski, A.; Dridi, K.; Hesthaven, J. S. (2001): Convergent Cartesian Grid Methods for Maxwell's Equa-

tions in Complex Geometries, *J. Comput. Phys.* **170**, pp. 39-80.

Hassan, O.; Morgan, K.; Jones, J.; Larwood, B.; Weatherill, N. P. (2004): Parallel 3D Time-Domain Electromagnetic Scattering Simulations on Unstructured Meshes, *CMES: Computer Modeling in Engineering & Sciences*, vol. 5, no. 5, pp. 383-394.

Hesthaven, J. S. (2000): Spectral Penalty Methods, *Appl. Numer. Math.* **33**, pp. 23-41.

Hesthaven, J. S.; Gottlieb, D. (1999): Stable Spectral Methods for Conservation Laws on Triangles with Unstructured Grids, *Comput. Methods Appl. Mech. Engin.* **175**, pp. 361-381.

Hesthaven, J. S.; Teng, C. H. (2000): Stable Spectral Methods on Tetrahedral Elements, *SIAM J. Sci. Comput.* **21**, pp. 2352-2380.

Hesthaven, J. S.; Warburton, T. (2001): High-Order/Spectral Methods on Unstructured Grids. I. Time-Domain Solution of Maxwell's Equations. *J. Comput. Phys.* **181**, pp. 186-221.

Jose, P.; Kanapady, R.; Tamma, K. K. (2004): Transform Domain Based Hybrid Element Formulations for Transient Electromagnetic Field Computations, *CMES: Computer Modeling in Engineering & Sciences*, vol. 5, no. 5, pp. 409-422.

Karniadakis, G. E.; Sherwin, S. J. (1999): Spectral/*hp* Element Methods for CFD. *Numerical Mathematics and Scientific Computation*. Clarendon Press, Oxford.

Koornwinder, T. (1975): Two-variable Analogues of the Classical Orthogonal Polynomials in "Theory and Application of Special Functions", R.A. Askey ed., Academic Press, pp. 435-495.

Kopriva, D. A.; Woodruff, S. L.; Hussaini, M. Y. (2000): Discontinuous Spectral Element Approximation of Maxwell's Equations. In Discontinuous Galerkin Methods: Theory, Computation and Applications. B. Cockburn, G. E. Karniadakis, and C.W. Shu (Eds). Lecture Notes in *Computational Science and Engineering* **11**, Springer Verlag, New York. pp. 355-362.

Kopriva, D. A.; Woodruff, S. L.; Hussaini, M. Y. (2002): Computation fo Electromagnetic Scattering with a Non-Conforming Discontinuous Spectral Element Method, *Int. J. Num. Meth. Engin.* **53**, pp. 105-122.

Kreiss, H. O.; Oliger, J. (1972): Comparison of Accurate Methods for the Integration of Hyperbolic Problems, *Tellus* **24**, pp. 199-215.

Mohammadian, A. H.; Shankar, V.; Hall, W. F. (1991): Computation of Electromagnetic Scattering and Radiation using a Time-Domain Finite-Volume Discretization Procedure, *Comput. Phys. Comm.* **68**, pp. 175-196.

Nambura, R. R.; Mark, E. R.; Clarke, J. A. (2004): Scalable Electromegnetic Simulation Environments, *CMES: Computer Modeling in Engineering & Sciences*, vol. 5, no. 5, 443-454.

Proriol, J. (1957): Sur une Famille de Polynomes à deux Variables Orthogonaux dans un Triangle, *C. R. Acad. Sci. Paris* **257**, pp. 2459-2461.

Rao, S. M. (1999): Time Domain Electromagnetics. Academic Press, San Diego.

Shore, R. (2000): Hanscom Airforce Base, MA, USA. Private Communication.

Szegö, G. (1939): Orthogonal Polynomials. *Colloquium Publications* **23**, American Mathematical Society, Providence, RI.

Taflove, A. (1995): Computational Electrodynamics. The Finite-Difference Time-Domain Method. Artech House, Boston.

Turkel, E.; Yefet, A. (2000): On the Construction of a High-Order Difference Scheme for Complex Domains in a Cartesian Grid, *Appl. Numer. Math.* **33**, pp. 113-124.

Volakis, J. L. (1992): Benchmark Plate Radar Targets for the Validation of Computational Electromagnetics Programs, *IEEE Antennas Propagat. Mag.* **34**, pp. 52-56.

Warburton, T. (2000): Application of the Discontinuous Galerkin Method to Maxwell's Equations Using Unstructured Polymorphic hp-finite Elements. In Discontinuous Galerkin Methods: Theory, Computation and Applications. B. Cockburn, G. E. Karniadakis, and C.W. Shu (Eds). *Lecture Notes in Computational Science and Engineering* **11**, Springer Verlag, New York. pp. 451-458.

Yang, B.; Hesthaven, J. S. (1999): A Pseudospectral Method for Time-Domain Computation of Electromagnetic Scattering by Bodies of Revolution, *IEEE Trans. Antennas Propaga.*, **47**, pp. 132-141.

Yefet, A.; Petropoulos, P. G. (2001): A Staggered Fourth-Order Accurate Explicit Finite Difference Scheme for the Time-Domain Maxwell's Equations, *J. Comput. Phys.* **168**, pp. 286-315.

Yefet, A.; Turkel, E. (2000): Fourth-Order Compact Implicit Method for the Maxwell Equations with Discontinuous Coefficients, *Appl. Numer. Math.* **33**, pp. 125-134.

Xie Z.; Chan, C.-H.; Zhang, B. (2002): An Explicit Fourth-Order Orthogonal Curvilinear Staggered-Grid FDTD Method for Maxwell's Equations, *J. Comput. Phys.* **175**, pp. 739-763.